IEEE Access
Multidisciplinary ⋮ Rapid Review ⋮ Open Access Journal

Received 13 May 2024, accepted 20 May 2024, date of publication 22 May 2024, date of current version 30 May 2024.

Digital Object Identifier 10.1109/ACCESS.2024.3404142

RESEARCH ARTICLE

Frequency Domain Analysis of a Dynamic Wireless Transfer System for Electric Vehicles

MINCUI LIANG, KHALIL EL KHAMLICHI DRISSI, (Senior Member, IEEE), AND CHRISTOPHE PASQUIER

Clermont Auvergne INP, CNRS, Institut Pascal, Université Clermont Auvergne, 63000 Clermont–Ferrand, France

Corresponding author: Mincui Liang (mincui.liang@uca.fr)

This work was supported in part by the International Research Center "Innovation Transportation and Production Systems" under Grant I-SITE CAP 20-25.

ABSTRACT Dynamic Wireless Power Transfer (DWPT) is a revolutionary technology for developing an autonomic electromobility transport system. A robust control method is essential for maximum power transfer with high efficiencies and the safe operation of the DWPT systems. This paper developed a frequency domain model of a series-series wireless power transfer system to thoroughly analyze how different control parameters affect the system performances under dynamic situations. For the first time, the power triangle phenomenon associated with the proposed optimum frequencies of a DWPT system is discovered to reveal the causal relationship between frequency, phase shift, and power. The theoretical performances of the proposed optimum frequencies are well aligned with the results of simulation and experiments, with 83% of the normalized root mean square errors less than 2%.

INDEX TERMS Dynamic wireless power transfer, electric vehicle, frequency-domain representation, optimum frequencies, wireless power transfer.

I. INTRODUCTION

In recent years, Electric Vehicles (EVs) have steadily gained a foothold in the global vehicle market. According to the latest data released by the International Energy Agency (IEA) [1], the sales of global EVs reached 13.9 million units in 2023, with a year-over-year growth rate of 35%, equating to a market penetration rate of 18%. While the price and range of EVs are already comparable to conventional vehicles, the charging of EVs continues to remain one of the major obstacles to the further uptake of EVs, given that the fastest charging still takes over half an hour to charge an EV's battery from empty to full. Building more charging stations would not ease the problem as long as it cannot catch up with the growth rate of the global EV market, especially if the market develops as projected by RMI in a recent study, potentially reaching 86% of global vehicle sales by 2030 [2]. Dynamic Wireless Charging (DWC), or Dynamic Wireless Power Transfer (DWPT), could be a viable solution to overcome the EV charging issues [3], [4]. The DWPT systems charge EVs while driving, providing unlimited and unplugged electromobility (e-mobility) without recharging hassles for EVs. This could potentially reshape the future of e-mobility for all types of vehicles.

On the other hand, although the first commercialized DWPT system was already unveiled in 2009 [5], the commercialization of the technology has still been challenged both technically and commercially due to its relatively low efficiency and high costs as the consequence of using loosely coupled coils. Many efforts have been made to address these problems, including the high-frequency Resonance Inductive WPT (RI-WPT) technology ranging from 79 kHz to 90 kHz, as regulated in the standard IEC 61980 [6], which has been widely studied during the past decade [7], [8]. Since the power transfer using the RI-WPT is sensitive to the choice of operating frequencies, frequency control naturally becomes one of the main control strategies in the field [9], [10], [11]. However, the operation of the systems

The associate editor coordinating the review of this manuscript and approving it for publication was Alon Kuperman.

proves to be very challenging as it is practically difficult to determine the optimum operating frequencies in such a short period. Moreover, the optimum operating frequencies change dynamically along with the changing coupling coefficients of the systems when an EV moves.

Series-Series WPT (SSWPT) is one of the most studied RI-WPT technologies in the research field since the SSWPT has a load-independent primary compensation capacitance [12] and is cost-effective for high-power applications [7]. Therefore, it makes SSWPT more suitable for DWPT applications utilized on EVs compared to the other mono-resonant compensation topologies such as series-parallel (SP), parallel-series (PS), and parallel-parallel (PP). The operation of an SSWPT system can be straightforwardly optimized by frequency or phase shift control [13], [14] as frequency, phase shift, and power form a cause-and-effect relationship in the system. One of the widely researched optimum frequencies is the Zero Phase Angle Frequency (ZPAF) of the input impedance, [12], [15], since it can reduce the reactive input power of the DWPT system, leading to nearly maximum power with high efficiency [16]. Due to the frequency bifurcation phenomenon, more than one ZPAF exists. Therefore, optimum frequency sweeping is introduced to track the ZPAFs by monitoring the out-phase ratio, starting from an initial frequency close to the resonance frequency of the primary resonance tank [17]. However, there is still a lack of principles behind the selection of the ZPAFs, the initial frequency for ZPAF sweeping, and the choice of the operating limits of coupling coefficients. Besides, most studies considered the SSWPT systems symmetric, meaning that the ratio between the primary and the secondary resonance frequency is assumed to equal 1 when calculating the ZPAFs [12], [18]. This is highly impractical since, with a high probability, future EVs would use different regulated receiver coils from different providers but share the same transmitter coils buried under the road. Although it is possible to maintain the ratio by alternating the capacitor values from the secondary side, there is still an absence of some significant information about the impact of different ratios on the operating limits of coupling coefficients and the range of the operating frequencies and phase shifts.

To fill the research gaps, we conducted a thorough Frequency Domain (FD) analysis with steady-state First Harmonic Approximation (FHA) [19] of a general SSWPT system, for the first time, to systematically understand different phase shifts and optimum frequencies presented in the system and make an in-depth comparison of their performances under different misalignment situations with respect to power and energy efficiencies. Firstly, we discussed the limits of coupling coefficients and the range of optimum frequencies for operation in DWPT applications with an unbalanced ratio of the primary and the secondary resonance frequencies. Secondly, we proposed a ZPAF of the output impedance as an alternative ZPAF of the input impedance with slightly better performance for DWPT. Thirdly, we introduced the power triangle formed by the ZPAF of input impedance, the ZPAF of output impedance, and the peak power frequency to expand the bandwidth of the control variables for DWPT operation. This could provide the readers valuable insights into understanding the relationship between frequency, phase shift and power, and lay a foundation for developing robust control strategies for practical DWPT applications.

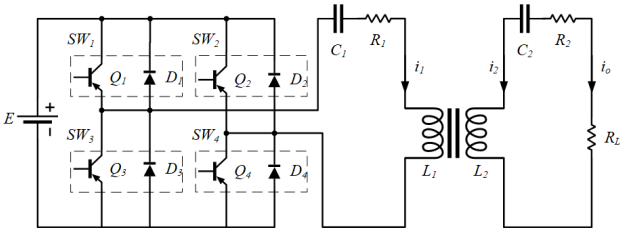

FIGURE 1. The circuit diagram of an SSWPT compensation network [20].

The rest of the paper is organized as follows. Section II introduces the frequency domain modeling of a general SSWPT system. Section III proposes respective optimum frequencies and the ways to find them. Section IV presents detailed theoretical results on the system performances and control parameters relative to the optimum frequencies discussed in Section II. The results are then further validated by simulation and experiments in Section V. Section VI concludes the paper with the achievements and suggestions for future studies.

II. FREQUENCY DOMAIN MODELING OF SSWPT

An SSWPT circuit consists of a full bridge inverter with four MOSFETs, SW_1 to SW_4, converting a DC voltage source, E, to an AC voltage source, two identical capacitors on the primary and secondary sides, C_1 and C_2, and two loosely coupled coils, L_1 and L_2, transferring energy from the primary side to power a resistive load, R_L, on the secondary side. R_1 and R_2 are the equivalent losses in the primary and secondary coils respectively. They are the main energy dissipation in the circuit apart from the switching losses which are not considered in this paper. The circuit diagram of the SSWPT is shown in Figure 1.

The normalized equivalent circuits of the SSWPT system with mutual inductance are shown in Figure 2. The upper one, Figure 2a, is the time-domain FHA representation and the lower one, Figure 2b, is its equivalent FD representation. The normalized equivalent AC voltage source is the fundamental sine wave component of the square wave, given as $x_s = \frac{4}{\pi}\cos(\theta_n)$, normalized by the value of the DC voltage source, E, where θ_n is the normalized operating angle, $\theta_n = \omega_{r1}t$.

In terms of normalization, there are four main characteristic parameters of the SSWPT circuit, including two resonant angular frequencies of the primary and secondary resonance tank, $\omega_{r1} = \frac{1}{\sqrt{L_1C_1}}$ and $\omega_{r2} = \frac{1}{\sqrt{L_2C_2}}$, and two characteristic impedances in the primary and secondary circuits, $Z_1 = \sqrt{\frac{L_1}{C_1}}$ and $Z_2 = \sqrt{\frac{L_2}{C_2}}$, respectively. In addition, extra dimensionless parameters need to be pre-defined to

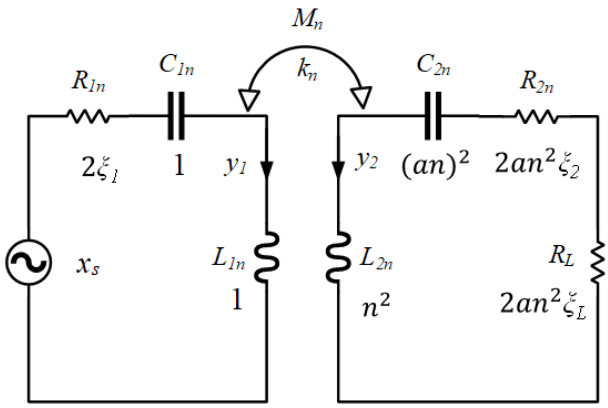

(a) The normalized equivalent circuit of an SSWPT with mutual inductance.

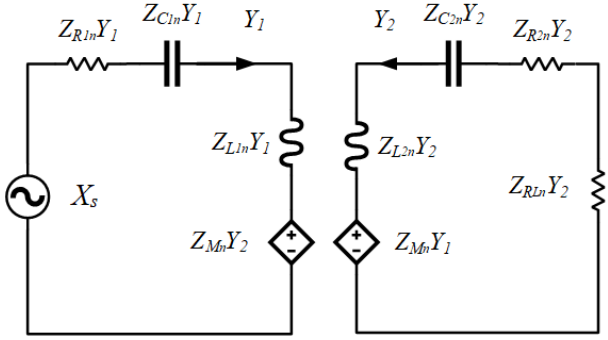

(b) The frequency-domain representation of the normalized equivalent circuit.

FIGURE 2. The normalized equivalent circuit of the SSWPT system.

ensure the scalability of the theoretical model. n^2 is the ratio of two inductors, $n^2 = \frac{L_2}{L_1}$; a is the ratio of primary and secondary resonant frequencies, $a = \frac{\omega_{r2}}{\omega_{r1}}$; k is the coupling coefficient, $k = \frac{M}{\sqrt{L_1 L_2}}$; X_1 and X_2 are dimensionless voltages across C_1 and C_2, $X_{1,2} = \frac{V_{C_{1,2}}}{E}$; Y_1 and Y_2 are dimensionless currents through L_1 and L_2, $Y_{1,2} = \frac{Z_1}{E} I_{1,2}$; X_{in} is the equivalent normalized input voltage in FD representation, $X_{in} = \frac{4}{\pi}\angle 0$; and the Root-Mean-Square (RMS) value of the equivalent normalized input voltage is given as $X_{in_{RMS}} = \frac{2\sqrt{2}}{\pi}$. All the circuit impedances are normalized by the characteristic impedance of the primary resonance tank, Z_1. The steady-state relationship of the SSWPT in the FD representation with dimensionless elements is given in a matrix form as (1).

$$\begin{bmatrix} Z_{p_n} & Z_{M_n} \\ Z_{M_n} & Z_{s_n} \end{bmatrix} \begin{bmatrix} Y_1 \\ Y_2 \end{bmatrix} = \begin{bmatrix} X_{in_{RMS}} \\ 0 \end{bmatrix} \tag{1}$$

where, Z_{p_n} is the normalized primary impedance, $Z_{p_n} = Z_{R_{1_n}} + Z_{C_{1_n}} + Z_{L_{1_n}}$; Z_{s_n} is the normalized secondary impedance, $Z_{s_n} = Z_{R_{2_n}} + Z_{R_{L_n}} + Z_{C_{2_n}} + Z_{L_{2_n}}$; $Z_{R_{1_n}}$ and $Z_{R_{2_n}}$ are the normalized impedances of the primary and secondary equivalent resistors, $Z_{R_{1_n}} = \frac{R_1}{2Z_1} = 2\zeta_1$ and $Z_{R_{2_n}} = \frac{R_2}{2Z_1} = 2an^2\zeta_2$; $Z_{L_{1_n}}$ and $Z_{L_{2_n}}$ are the normalized impedances of the primary and secondary inductors, $Z_{L_{1_n}} = j\omega_n$ and $Z_{L_{2_n}} = n^2 j\omega_n$; $Z_{C_{1_n}}$ and $Z_{C_{2_n}}$ are the normalized impedances of the primary and secondary capacitors, $Z_{C_{1_n}} = -\frac{j}{\omega_n}$ and $Z_{C_{2_n}} = -a^2 n^2 \frac{j}{\omega_n}$; $Z_{R_{L_n}}$ is the normalized impedance of the load resistance, $Z_{R_{L_n}} = \frac{R_L}{2Z_1} = 2an^2\zeta_L$; Z_{M_n} is the normalized impedance of the mutual inductor, $Z_{M_n} = jkn\omega_n$.

Impedance represents the relationship between voltage and current, such as the phase shift between voltage and current. There are three main phase shifts presented in the SSWPT system, i.e. (1) the phase shift, θ_1, between the normalized input voltage, X_{in}, and the normalized primary current, Y_1, which is related to the normalized input impedance, Z_{in_n}, (2) the phase shift, θ_2, between the normalized input voltage, X_{in}, and the normalized secondary current, Y_2, which is associated with the normalized output impedance, Z_{out_n}, and (3) the phase shift, θ_{12}, calculated from Z_{12_n}, between the normalized primary current, Y_1, and the secondary current, Y_2, or equally between the normalized primary capacitor voltage, X_1, and the normalized secondary capacitor voltage, X_2, which is the difference between θ_1 and θ_2 as well. The mathematical relationships of Z_{in_n}, Z_{out_n} and Z_{12_n} are given in (2).

$$\begin{cases} Z_{in_n} = \dfrac{X_{in_{RMS}}}{Y_1} = Z_{p_n} + Z_{r_n} \\ Z_{out_n} = \dfrac{X_{in_{RMS}}}{Y_2} = \dfrac{-Z_{p_n} Z_{s_n} + {Z_{M_n}}^2}{Z_{M_n}} \\ Z_{12_n} = \dfrac{Y_1}{Y_2} = \dfrac{X_1}{X_2} = -\dfrac{Z_{s_n}}{Z_{M_n}} \end{cases} \tag{2}$$

where Z_{r_n} is the normalized primary reflected load impedance [21], $Z_{r_n} = -\frac{{Z_{M_n}}^2}{Z_{s_n}}$.

By regulating these phase shifts, we are able to find the optimum frequencies to achieve the desired performances of the SSWPT systems during operation.

III. THE PROPOSED OPTIMUM FREQUENCIES

In this section, we present theoretical ways to find four types of optimum frequencies of the SSWPT systems that can be used to optimize the system performances, namely Primary Zero Phase Angle Frequency (PZPAF), Secondary Zero Phase Angle Frequency (SZPAF), Peak Input Power Frequency (PIPF) and Peak Output Power Frequency (POPF).

A. PRIMARY ZERO PHASE ANGLE FREQUENCY

The normalized input impedance in (2), Z_{in_n}, is a complex algebraic expression containing the imaginary part and the real part. The PZPAF can be found by setting the imaginary part of the normalized input impedance, $\Im Z_{in_n}$, equal to zero, as given in (3). More specifically, by setting its numerator, $N_{in}(k, \omega_n, \zeta_s, a)$, equal to zero, we get a sextic equation without the terms of odd degrees as (4), which means there is

more than one PZPAF in practice.

$$\Im Z_{in_n} = -j\frac{N_{in}(k,\omega_n,\zeta_s,a)}{\omega_n[(2a\zeta_s)^2\omega_n{}^2+(\omega_n{}^2-a^2)^2]} \quad (3)$$

$$N_{in}(k,\omega_n,\zeta_s,a) = (1-k^2)\omega_n{}^6+(a^2(4\zeta_s{}^2+k^2-2)-1)\omega_n{}^4 + [a^4-a^2(4\zeta_s{}^2-2)]\omega_n{}^2-a^4=0 \quad (4)$$

where ζ_s is the sum of the normalized secondary equivalent resistance and the load resistance, $\zeta_s = \zeta_2 + \zeta_L$.

Since the roots carry physical meanings, only three positive ones are considered. Especially, three distinct roots exist when its discriminant is greater than zero for k greater than 0.1901, as shown in Figure 3. One of the roots is real for the entire range of k, notated as ω_{3_n}, which however increases exponentially when k approaches 1. Therefore, a constraint on the maximum control frequency should be imposed practically for frequency sweeping on ω_{3_n} when k is high. The other two roots, ω_{1_n} and ω_{2_n}, are only real for a certain range of k, depending on a and ζ_s. Thus, in the remainder of the paper, the analysis of the SSWPT system is limited to the grey rectangular region in Figure 3, where the normalized frequency ranges from 0.7 to 1.6, limited by the FHA valid frequency range, and the coupling coefficient is from 0.11 to 0.581. The lower limit of the coupling coefficient, k_{min}, is chosen to avoid low coupling coefficient operation causing high primary current and the upper limit, k_{max}, is the maximum that the lab-made coils can provide. Moreover, the lower limit of the coupling coefficient, k_L, is set to 0.1901 when ω_{1_n} and ω_{2_n} are the control frequencies.

B. SECONDARY ZERO PHASE ANGLE FREQUENCY

Similar to the PZPAF, the SZPAF can be found by setting the imaginary part of the normalized output impedance, $\Im Z_{out_n}$, which is extracted from the complex algebraic expression of Z_{out_n} in (2) and given in (5), equal to zero to achieve nearly maximum output power by finding balance between maximizing the RMS value of the normalized output current, Y_2, as expressed in (10), and keeping the ZPA condition between the input voltage and output current. More specifically, by setting its numerator, $N_{out}(k,\omega_n,\zeta_1,\zeta_s,a)$, equal to zero, we get a bi-quadratic equation as (6), which can be solved as a quadratic equation by the method of supposition, i.e. substituting the square of the variable into a new variable.

$$\Im Z_{out_n} = -jn\frac{N_{out}(k,\omega_n,\zeta_1,\zeta_s,a)}{k\omega_n{}^3} \quad (5)$$

$$N_{out}(k,\omega_n,\zeta_1,\zeta_s,a) = (1-k^2)\omega_n{}^4-(4a\zeta_1\zeta_s + a^2+1)\omega_n{}^2+a^2=0 \quad (6)$$

Although four real roots exist as the discriminant of (6) is always greater than zero, only two positive ones are considered due to their inherited physical meanings. The two SZPAFs are notated as ω_{4_n} for the root of lower value, given in (7), and ω_{5_n} for the root of higher value, given in (8).

$$\omega_{4_n} = \sqrt{\frac{4a\zeta_1\zeta_s+a^2+1-\sqrt{(4a\zeta_1\zeta_s+a^2+1)^2-4a^2(1-k^2)}}{2(1-k^2)}} \quad (7)$$

$$\omega_{5_n} = \sqrt{\frac{4a\zeta_1\zeta_s+a^2+1+\sqrt{(4a\zeta_1\zeta_s+a^2+1)^2-4a^2(1-k^2)}}{2(1-k^2)}} \quad (8)$$

C. PEAK INPUT POWER FREQUENCY

The PIPF is the normalized frequency corresponding to the peak value of the normalized input power, P_{in_n}, given in (9), which is the square of the RMS value of the normalized primary current, Y_1, multiplied by the real part of the normalized input impedance, $\Re Z_{in_n}$.

$$P_{in_n} = |Y_1|^2\Re Z_{in_n} \quad (9)$$

where Y_1 is the normalized primary current in the FD representation, $Y_1 = \frac{X_{in_{RMS}}}{Z_{in_n}}$.

The PIPFs are practically solved by using numerical methods. A pseudo-code example is given in Algorithm 1. For each k, two PIPFs exist for the SSWPT system. In this paper, the ones with lower values are notated as ω_{6_n} and those with higher values are notated as ω_{7_n}.

Algorithm 1 Finding *PIPFs*

Input:
ω_n - An array of normalized frequencies
k_n - An array of coupling coefficients
Output:
PIPFs - An array of resulted *PIPFs*

```
initialize PIPFs as empty list
for k in k_n do
    for ω in ω_n do
        calculate P_in_n
    end for
    for ω in ω_n do
        initialize index as empty list
        findpeaks(P_in_n)
        index = ω
    end for
    PIPFs = union(PIPFs, index)
end for
return PIPFs
```

D. PEAK OUTPUT POWER FREQUENCY

Analogously, the POPF corresponds to the peak value of the normalized output power, P_{out_n}, expressed in (10), equating to the square of the RMS value of the normalized secondary

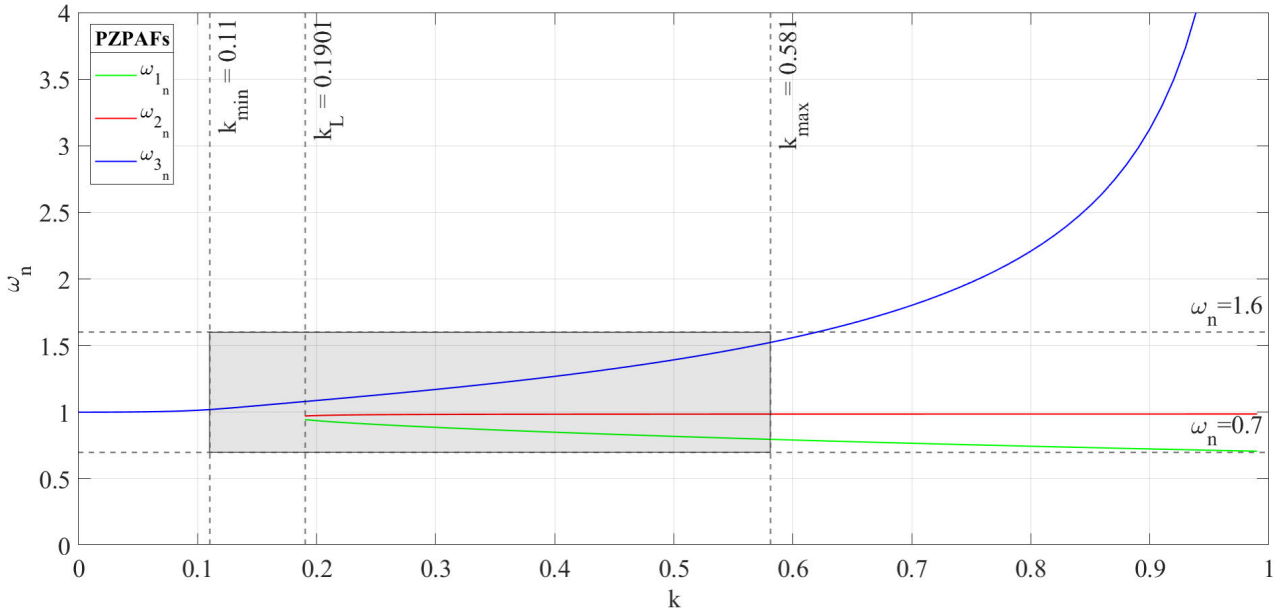

FIGURE 3. The three positive roots of the sextic equation for the range of k from 0 to 1.

TABLE 1. The key parameters of the SSWPT system.

L_1(μH)	L_2(μH)	C_1(nF)	C_2(nF)	$R_1(\Omega)$	$R_2(\Omega)$	$R_L(\Omega)$	$Z_1(\Omega)$
118.72	121.99	22	22	0.2537	0.2869	9.7988	73.4599

current, Y_2, multiplied by the normalized resistive load, Z_{L_n}.

$$P_{out_n} = 2an^2\zeta_L|Y_2|^2 \tag{10}$$

where Y_2 is the normalized secondary current in the FD representation, $Y_2 = \frac{X_{in_{RMS}}}{Z_{out_n}}$.

Similar to the PIPFs, two POPFs exist for the SSWPT system under each misalignment situation, which can be similarly calculated using Algorithm 1, except replacing P_{in_n} with P_{out_n}. The POPFs with lower and higher values are notated as ω_{8_n} and ω_{9_n}, respectively.

IV. THEORETICAL RESULTS

In this section, we use the equations presented in Section III to calculate the optimum frequencies, phase shifts, power, and energy efficiencies and compare their performances and mutual influences on the performances of the system, based on one experimental setup [22] corresponding to the SSWPT circuit in Section II. Table 1 lists the values of the main components of the experimental setup. The primary and secondary inductors, L_1 and L_2, are fabricated in the lab with slightly different values in self-inductance resulting in a ratio of a smaller than 1. Their self-inductance and mutual inductance under different misalignment situations are cross-validated and verified in our previous research [22]. The two capacitors, C_1 and C_2, and the resistive load, R_L, are standard components purchased from the market.

A. SYSTEM PERFORMANCE

1) THE OPTIMUM FREQUENCIES

Based on the methods given in Section III, the proposed normalized optimum frequencies of the SSWPT system are calculated and given in Table 2. As illustrated in Figure 4, these normalized optimum frequencies are separated into three groups. Group A includes four normalized frequencies on the left-hand side, explicitly, ω_{1_n}, ω_{4_n}, ω_{6_n}, and ω_{8_n}. Group B includes four normalized frequencies on the right-hand side, i.e. ω_{3_n}, ω_{5_n}, ω_{7_n} and ω_{9_n}. ω_{2_n} is close to $a = 0.9865$ in the middle, being Group C alone.

Generally, the optimum frequencies in the same group have similar values. The average Normalized Root Mean Square Errors (NRMSEs) of Group A and Group B are 0.717% and 0.739% respectively, as given in Table 2. The PZPAFs, ω_{1_n} and ω_{2_n}, do not exist when k is smaller than k_L, specifically when $k = 0.11$ or 0.165. The differences between the PIPFs and POPFs are so small (less than 0.005) that they can almost be considered the same.

For all the coupling coefficients, the proposed optimum frequencies remain relatively in the same order across the frequency spectrum, as illustrated in Figure 5. Different optimum frequency types are highlighted in different colors. Note that one of the PZPAFs, ω_{2_n}, is close to a which is smaller than 1. Taking ω_{2_n} as a reference, all the optimum frequencies in group A are located on the left-hand side and all the optimum frequencies in group B are on the right-hand side, and they are nearly vertically symmetric. More specifically, the PZPAFs in Group A, ω_{1_n}, are the highest and thus the closest to ω_{2_n}, the SZPAFs, ω_{4_n}, are the lowest and hence located on the west most of the axis, and the PIPFs, ω_{6_n}, and the POPFs, ω_{n_8}, are located in between ω_{4_n} and ω_{1_n}, with

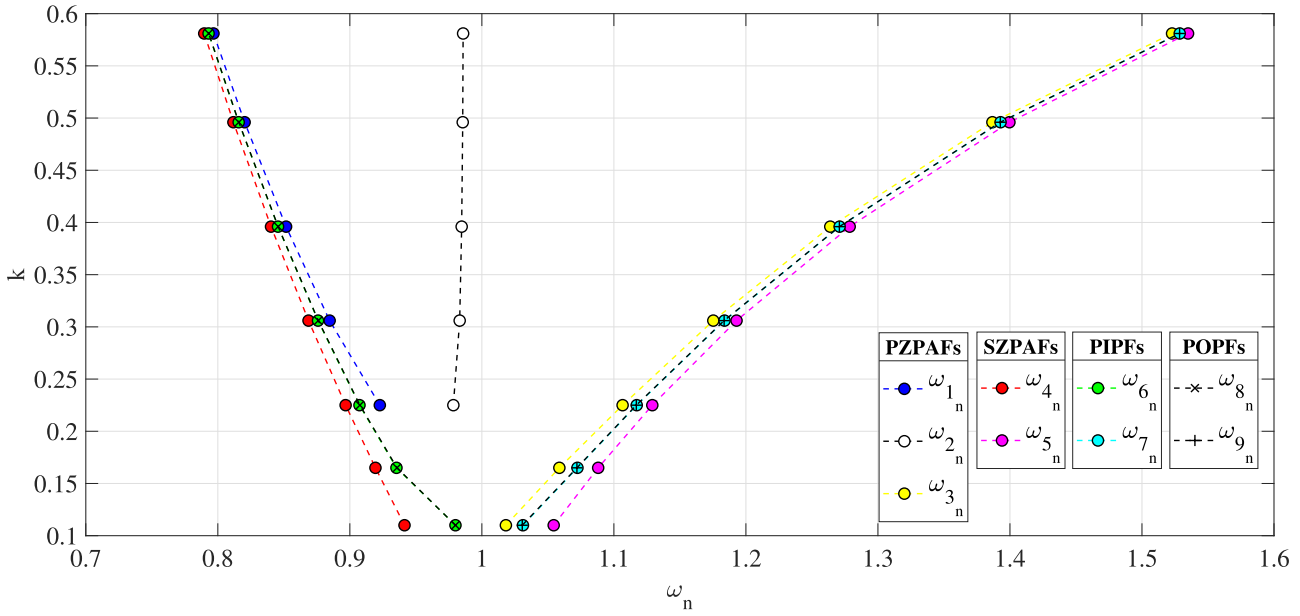

FIGURE 4. The proposed optimum frequencies.

TABLE 2. The proposed optimum frequencies.

k	k_1	k_2	k_3	k_4	k_5	k_6	k_7
	0.11	0.165	0.225	0.306	0.396	0.496	0.581
ω_{1_n}	NaN	NaN	0.9227	0.8847	0.8517	0.8203	0.7967
ω_{4_n}	0.9414	0.9194	0.8968	0.8687	0.8403	0.8118	0.7897
ω_{6_n}	0.9800	0.9353	0.9073	0.8759	0.8456	0.8158	0.7930
ω_{8_n}	0.9800	0.9357	0.9076	0.8761	0.8457	0.8159	0.7931
$\varepsilon(\%)$	1.820	0.759	0.923	0.567	0.403	0.301	0.248
ω_{2_n}	NaN	NaN	0.9784	0.9832	0.9847	0.9855	0.9858
ω_{3_n}	1.0182	1.0587	1.1066	1.1753	1.2639	1.3867	1.5228
ω_{5_n}	1.0544	1.0881	1.1291	1.1929	1.2786	1.3996	1.5349
ω_{7_n}	1.0311	1.0724	1.1173	1.1838	1.2710	1.3929	1.5286
ω_{9_n}	1.0306	1.0720	1.1170	1.1835	1.2708	1.3927	1.5285
$\varepsilon(\%)$	1.309	1.041	0.796	0.623	0.520	0.456	0.428

* Note: ε – NRMSE.

FIGURE 5. The relative order of the proposed optimum frequencies across the frequency spectrum.

ω_{6_n} slightly on the left meaning that the PIPFs in Group A are a little lower than the POPFs. On the contrary, the PZPAFs in Group B, ω_{3_n}, are the lowest and thus the closest to 1, the SZPAFs, ω_{5_n}, are the highest and hence located on the east most of the axis, and the PIPFs, ω_{7_n}, and the POPFs, ω_{9_n}, are in between ω_{3_n} and ω_{5_n}, with ω_{7_n} slightly on the right meaning that the PIPFs in group B are a little higher than the POPFs. This can provide useful guidance on the selection of the initial frequency, target frequency and approaching direction when conducting frequency sweeping.

2) INPUT AND OUTPUT IMPEDANCE

As presented in Figure 6, the PZPAFs, ω_{1_n}, ω_{2_n} and ω_{3_n}, are all located from left to right on the horizontal axis ($\Im Z_{in_n} = 0$), regardless of k. In Group A, the SZPAFs, PIPFs and POPFs are negative and the maximum absolute difference between the values is less than 0.1. On the contrary, in Group B, the corresponding SZPAFs, PIPFs and POPFs are positive and the maximum absolute difference is less than 0.06. The values of each frequency type in Group A and Group B are close to their original symmetry. In general, the PZPAFs, SZPAFs, PIPFs and POPFs have only small differences in $\Im Z_{in_n}$, and they follow the same order as described in Section IV-A1.

Similarly, the SZPAFs, ω_{4_n} and ω_{5_n}, are all located on the horizontal axis ($\Im Z_{out_n} = 0$), regardless of k, as shown in Figure 7. The $\Im Z_{out_n}$ of all proposed optimum frequencies are non-negative, with maximum absolute differences of less than 0.1 between them. The bigger the coupling coefficient, k, the smaller the difference in the values. The behavior of the optimum frequencies in Group A and Group B is similar to vertical symmetry in terms of the $\Im Z_{out_n}$.

3) EFFICIENCY

Efficiency is one of the key performance indicators of a DWPT system. It depends on the equivalent losses in the system given in (11), which is calculated as the ratio of $\Re Z_{r_n}$ to $\Re Z_{in_n}$ in the primary side multiplying the ratio of ζ_L to the sum of ζ_2 and ζ_L in the secondary side. Operating the system at the optimum frequencies leads to high system efficiencies, with the overall efficiencies higher than 91%, as shown in Figure 8. The system performs slightly better when operating at the frequencies of Group A than Group B since R_2 is slightly higher than R_1.

$$\eta = \frac{\Re Z_{r_n}}{\Re Z_{in_n}} \frac{\zeta_L}{(\zeta_2 + \zeta_L)} \tag{11}$$

B. CONTROL PARAMETER ANALYSIS

The ultimate control goal of an SSWPT system is to transfer power efficiently by controlling frequency, phase

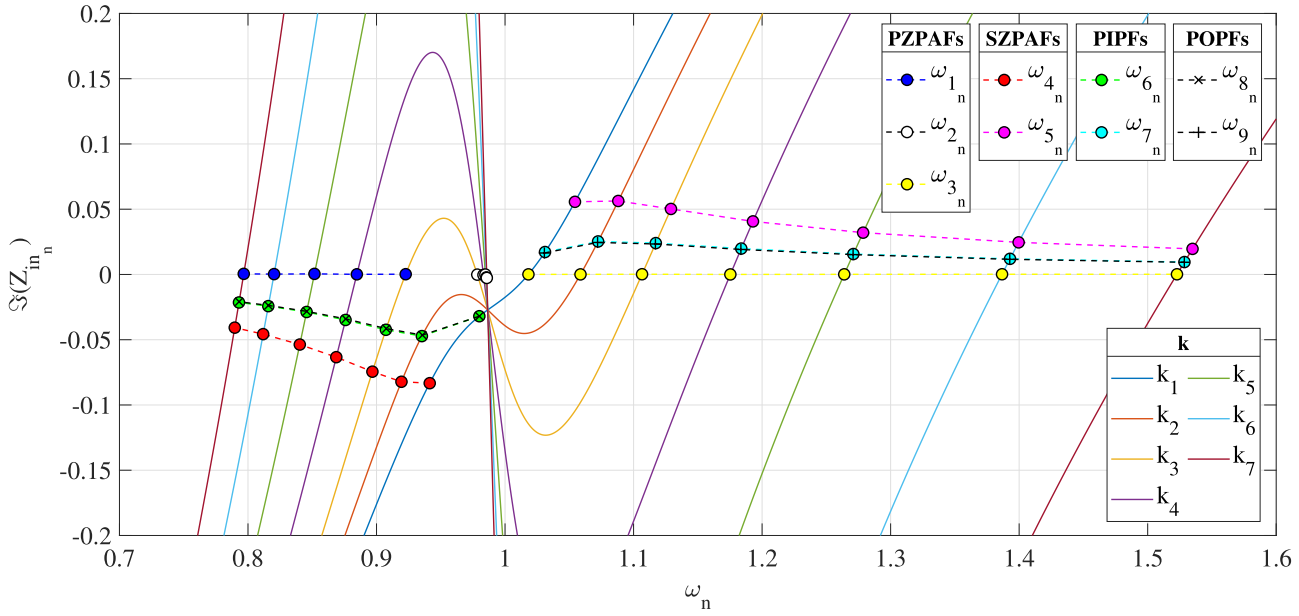

FIGURE 6. The normalized input impedance imaginary part.

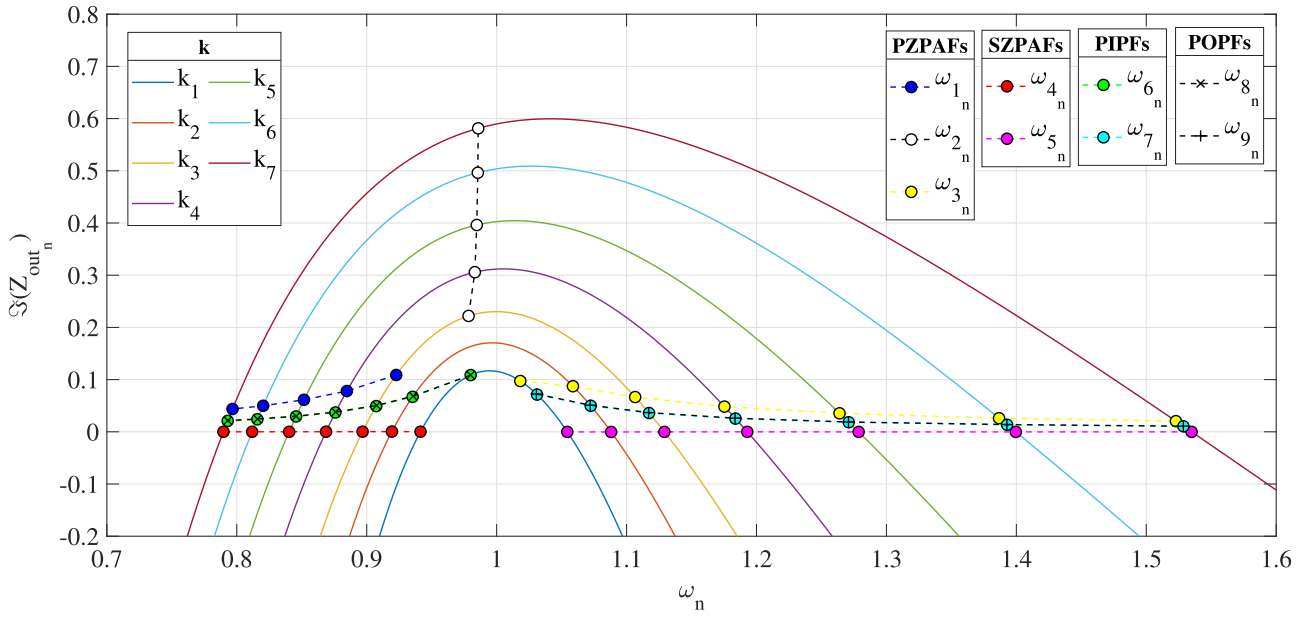

FIGURE 7. The normalized output impedance imaginary part.

shift, or both at the same time. The frequency and phase shift are convertible to each other. The relationship of each pair within frequency, phase shifts and power is discussed in this section. Theoretically, the system can be controlled from either the primary or secondary side by using different control parameters.

1) PHASE SHIFT AND FREQUENCY

The range of the phase angle, θ_1, is from $-90°$ to $90°$, as shown in Figure 9. The three types of PZPAFs, ω_{1_n}, ω_{2_n} and ω_{3_n}, cannot be distinguished from phase angles alone because they all satisfy the ZPA condition. Extra conditions are needed to determine the exact PZPAFs, such as the resulting frequencies, power, or the direction to approach the PZPAFs, i.e. θ_1 changing from negative to positive when zero crossing or vice versa. In Group A, θ_1 is negative, meaning that Y_1 is leading X_s and the Z_{in_n} is capacitive. On the contrary, the positive values of θ_1 in Group B indicate that Z_{in_n} is inductive, which is also one of the conditions to achieve Zero Voltage Switching (ZVS) [23]. As an overall trend, the differences in θ_1 at all the optimum frequencies decrease when k increases. The absolute values of θ_1 are the biggest in

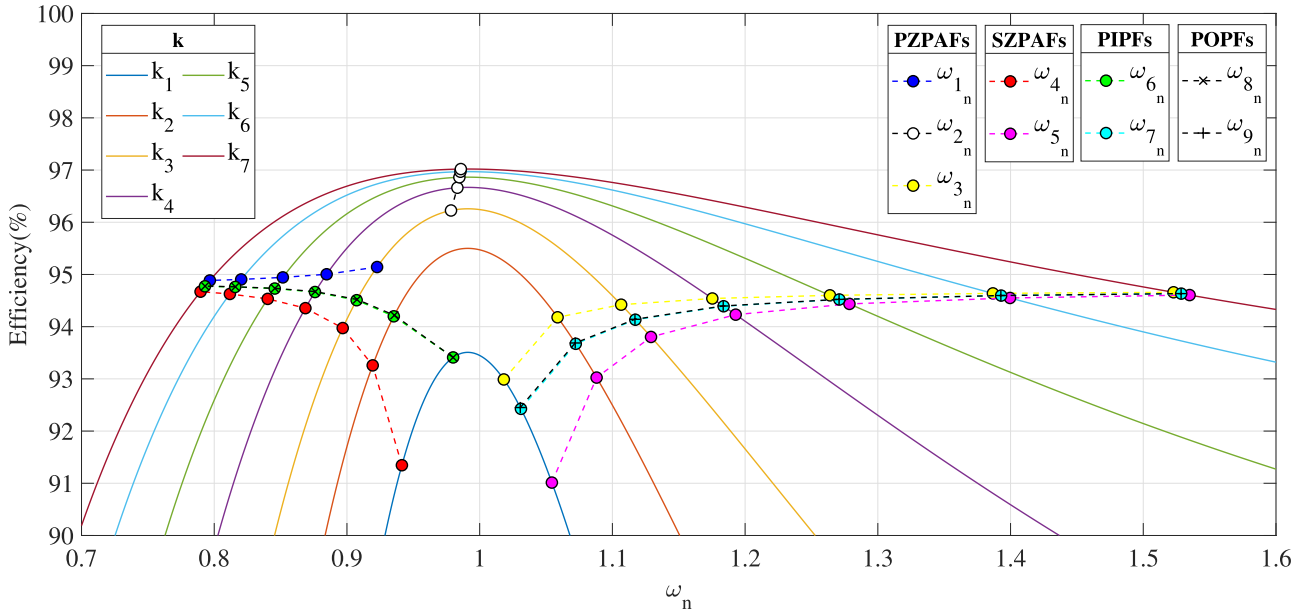

FIGURE 8. The efficiencies of the SSWPT system at the proposed optimum frequencies.

relation to the SZPAFs. Compared to the SZPAFs, θ_1 of the PIPFs and POPFs changes more modestly for all k. θ_1 can be used for primary control.

For all the optimum frequency types, θ_2 differs mostly at least 90° between Group A and Group B, as shown in Figure 10. The differences widen to approximately 180° when k increases. Especially for the SZPAFs, the differences between ω_{4_n} and ω_{5_n} are 180° all the time. At the other extreme, θ_2 is nearly 90° for ω_{2_n} under all misalignment conditions. Practically, wireless communication is required to send the data of Y_2 to the primary side, or vice versa.

The phase angle, θ_{12}, represents the phase shift between Y_1 and Y_2, is within the range of 0° to 180°. Y_1 and Y_2 are never in phase, as seen in Figure 11. Moreover, θ_{12} does not depend on k but the frequency given that the other system variables are fixed, as mentioned in Section IV. Therefore, θ_{12} and frequency are inter-convertible. When frequency increases, θ_{12} increases simultaneously. As shown in Figure 11, the leftmost point corresponds to ω_{4_n}, and therefore other optimum frequencies in Group A for the same k are on the right-hand side of ω_{4_n}. Oppositely, ω_{5_n} corresponds to the rightmost point of the optimum frequency spectrum, resulting in other optimum frequencies in Group B on its left-hand side. They are consistent with Figure 5. θ_{12} in Group A and Group B moves in opposite directions When k increases, meaning their differences become larger. When k equals 0.581, the difference reaches the extreme. In this situation, each normalized frequency has unique θ_{12}, and hence it can act as an additional condition to distinguish the optimum frequencies when there is more than one solution. Since it requires information from both sides, wireless communication is needed.

2) POWER AND FREQUENCY

Power is another equally important system performance indicator. The input and output power are calculated using (9) and (10) and visualized in Figure 12 and Figure 13, with the normalized optimum frequencies highlighted, respectively. For all k, the normalized output power is clearly proportional to the normalized input power in the SSWPT system. Due to low equivalent losses, they are very close to each other, indicating high overall efficiencies when operated at the proposed optimum frequencies, as shown in Figure 8.

The normalized input and output power of ω_{2_n} are too low to be used as the control frequencies. Particularly, when the coupling coefficient is equal to 0.581, the power is close to zero, even though their efficiency is high, as shown in Figure 8. Therefore, it is not recommended as the control frequency for power transfer. However, it could be still useful for other purposes such as soft shutdown, etc., instead of cutting off the power directly. According to the experimental setup, the ratio a is smaller than 1. Hence, when controlling with the proposed optimum frequencies, both the normalized input and output power of Group B are bigger than Group A. Furthermore, the corresponding amplitudes of the PZPAFs and SZPAFs on both sides are similar for both normalized input and output power, especially in the high coupling coefficient situations. The PIPFs and the POPFs correspond to the peak power frequencies as expected and the ranges for peak power tracking are between PZPAFs and SZPAFs.

3) POWER AND PHASE SHIFT

Figure 14, Figure 15, and Figure 16 present the relationships between the three main phase shifts and the normalized

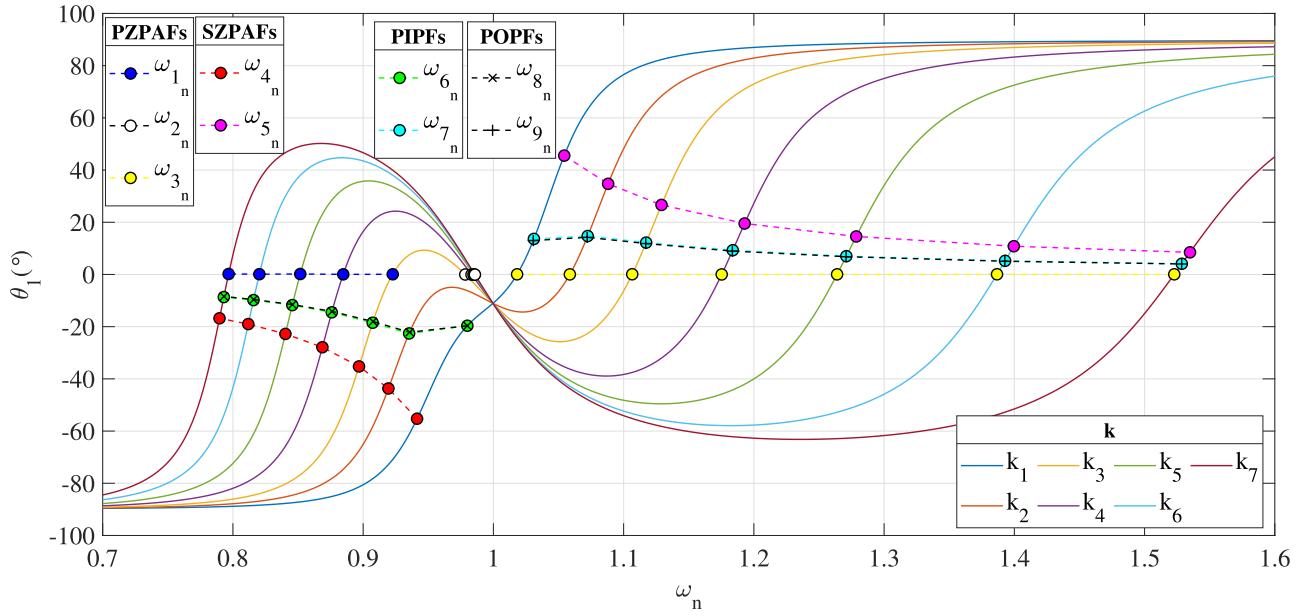

FIGURE 9. θ_1 with the highlighted optimum frequencies.

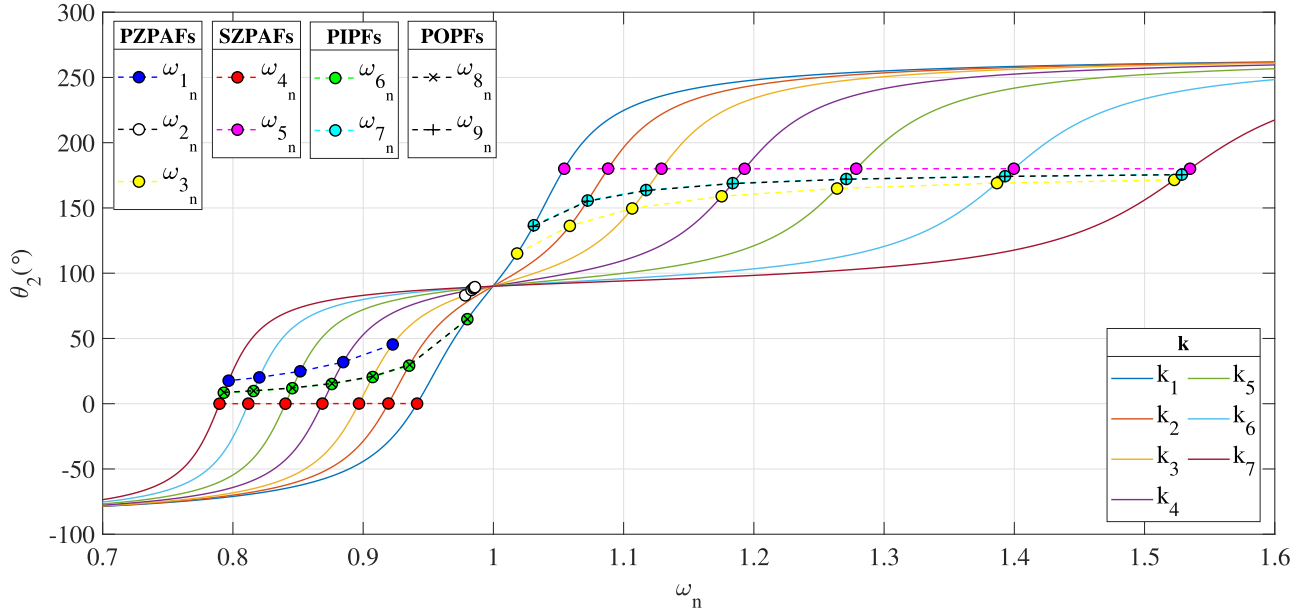

FIGURE 10. θ_2 with the highlighted optimum frequencies.

output power. Once the power is determined, depending on the coupling coefficient, the corresponding phase shifts can be considered as the control variable. The same optimum frequencies lead to the same normalized input and output power but three different types of phase shifts, namely, θ_1, θ_2, and θ_{12}.

As detailed in Figure 14, the prominent PZPAFs, with θ_1 equal to zero, are vertically aligned for all k, which is a good feature for DWPT as the controlling phase shifts do not need to change for different coupling coefficients, even though the output powers of the three types of PZPAFs are different. On the other hand, the SZPAFs are not far from the horizontal alignment, meaning that the normalized output power is almost constant for all k, however, the controlling phase shifts need to be tuned separately for each k. The PIPFs and POPFs lie in between the PZPAFs and SZPAFs. Controlling phase shifts between the PZPAFs and SZPAFs ensures that their output power is higher than the PZPAFs' and SZPAFs'. However, the normalized output power is not quite constant especially when k is low, when operating at the

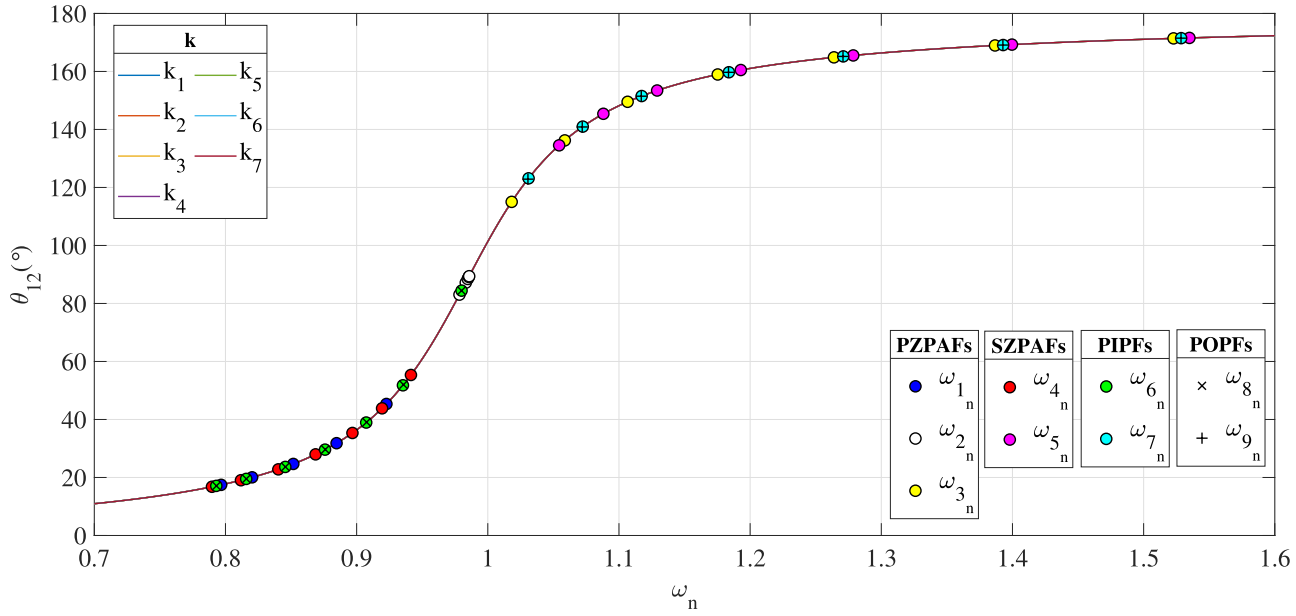

FIGURE 11. θ_{12} with the highlighted optimum frequencies.

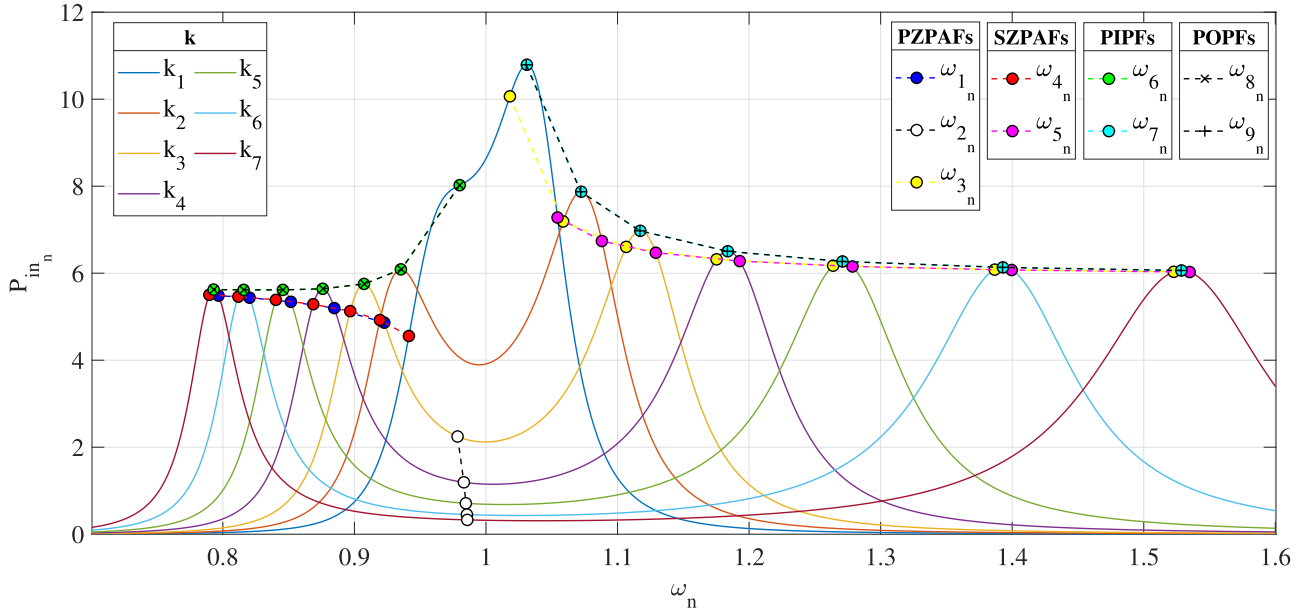

FIGURE 12. The normalized input power with the proposed optimum frequencies.

PIPFs and POPFs. Therefore, a limit on maximum operation power should be added.

The performance in Figure 15 is opposite to Figure 14. The normalized output power of the SZPAFs becomes vertically aligned, with θ_2 equal to zero but the difference in the normalized output power is smaller than the normalized output power of the PZPAFs, as shown in Figure 15. There is no peak surging issue for low k situations, which means the SZPAFs have a self-protection feature. On the contrary, the PZPAFs, PIPFs, and POPFs are close to the horizontal alignment, especially for Group A, but change dramatically when k becomes small, causing the peak surging issue.

In Figure 16, the relationship of the normalized output power and θ_{12} looks similar to Figure 13 because θ_{12} and the frequency are exchangeable. The two limits of the optimum power output are the θ_{12} corresponding to the PZPAF and the SZPAF respectively. Outside of the limits, the power starts decreasing for all k.

4) POWER TRIANGLE

When looking at Figure 12 and 13, one can easily observe there are some triangular areas with the PZPFs, SZPFs, and PIPFs (or POPFs) as vertices, which we refer to as "power triangles" since it forms the boundary of the potential

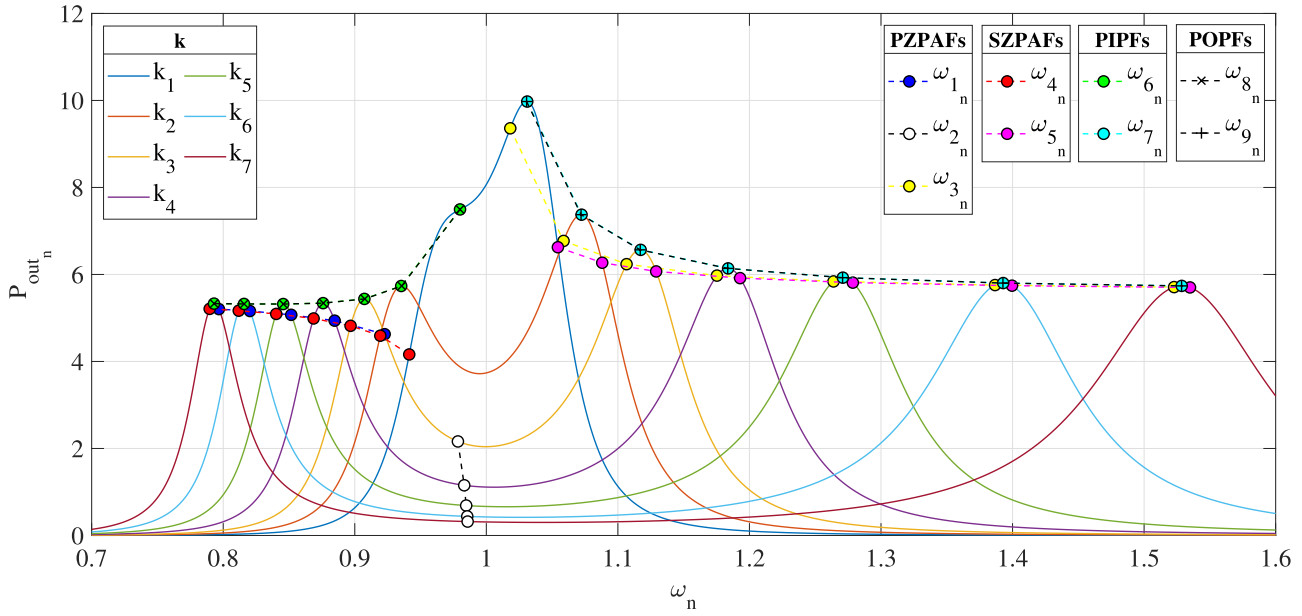

FIGURE 13. The normalized output power with the proposed optimum frequencies.

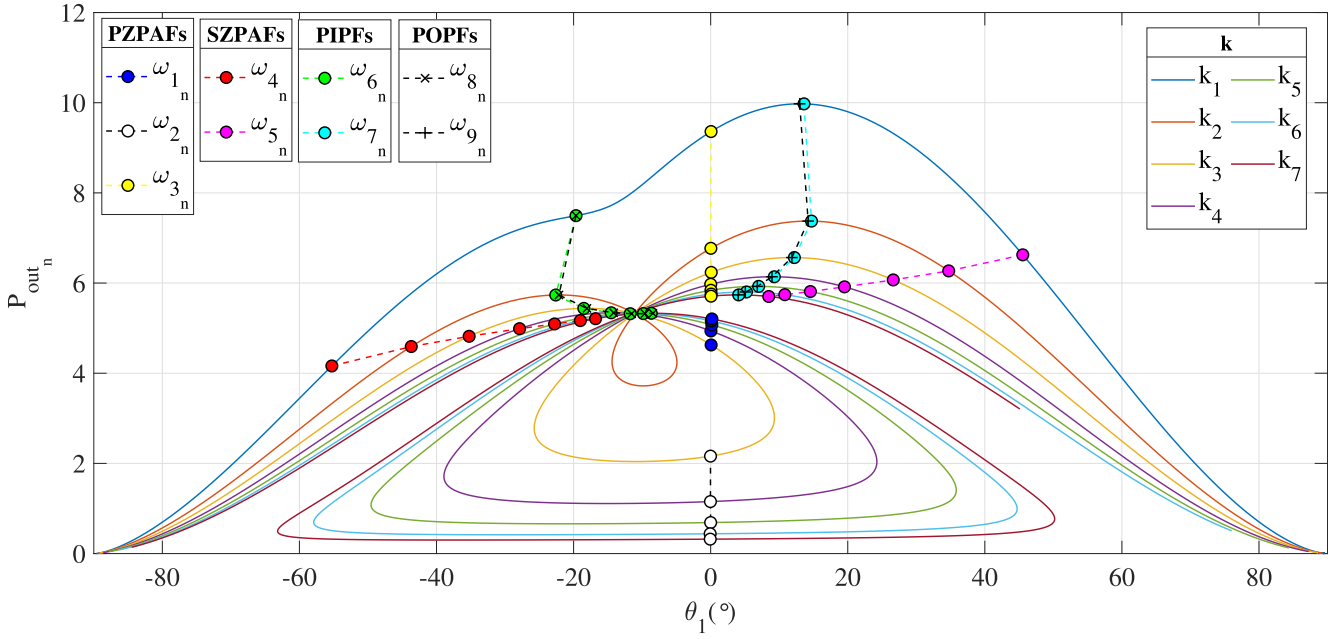

FIGURE 14. θ_1 and the normalized output power.

optimum frequencies for maximum power transfer. Therefore, tracking one optimum frequency becomes tracking a range of optimum frequencies for each k. Since the frequency can be converted to three different phase shifts, the relationships between power and three different phase shifts also inherit the power triangle phenomenon. To quantify the range of the potential optimum frequencies, a Modified Fractional BandWidth (MFBW) is calculated in (12), defined as the absolute bandwidth of the corresponding signal divided by the mean value of the corresponding signal between PIPFs and POPFs acting as the center frequency or phase shift.

$$MFBW = \frac{2|signal(PZPFs) - signal(SZPFs)|}{signal(PIPFs) + signal(POPFs)} \tag{12}$$

where *signal* refers to ω_{o_n}, θ_1, θ_2 or θ_{12}.

Taking k_3 in Figure 13 as an example, the two power triangles are formed by connecting the three power points corresponding to the PZPFs, SZPFs, and PIPFs (or POPFs) in Group A and Group B respectively, as shown in Figure 17. The related absolute bandwidths are the differences between

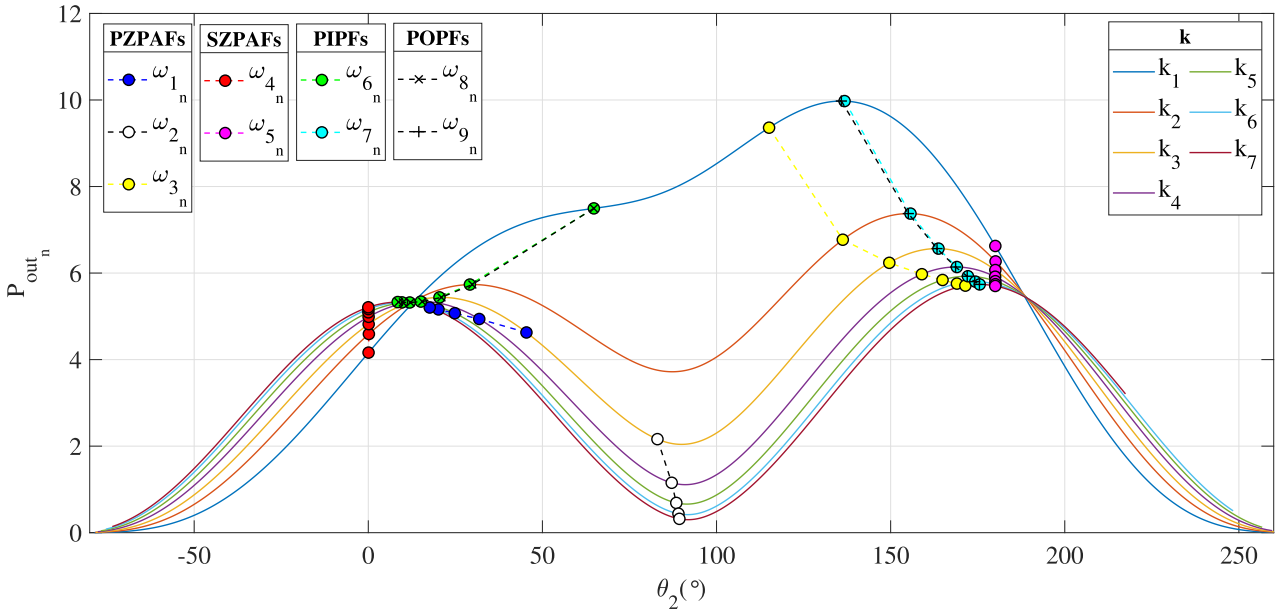

FIGURE 15. θ_2 and the normalized output power.

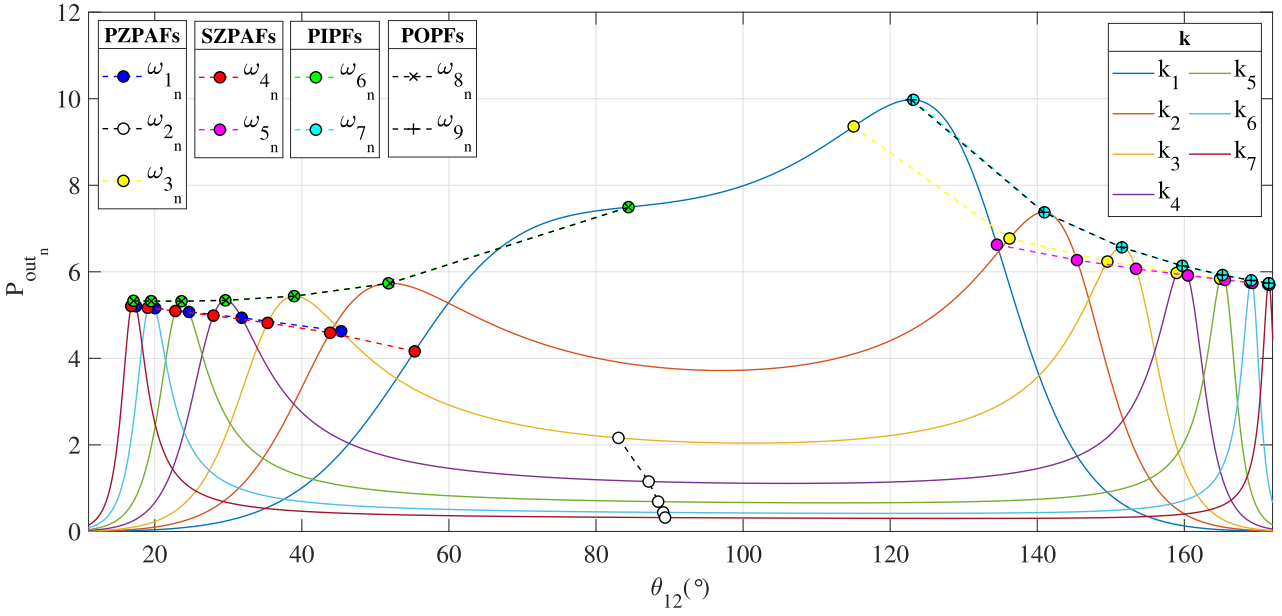

FIGURE 16. θ_{12} and the normalized output power.

PZPFs and SZPFs, i.e., between ω_{1_n} and ω_{4_n} in Group A and between ω_{3_n} and ω_{5_n} in Group B. Similarly, power triangle and bandwidth apply also to the power and phase shifts relationship as shown in Figure 14, 15 and 16. The detailed results are shown in Table 3. In general, MFBW becomes bigger when k is smaller, meaning that the range becomes wider. When there are ZPA situations, the range becomes extremely wide because the center frequency (or phase shift) is also close to zero, which is small compared to the absolute frequency (or phase shift), as shown in the third, fourth, and seventh rows of Table 3. Moreover, the bandwidth of frequency is smaller than the bandwidth of phase shift, which means phase shift control has a higher tolerance to power changes.

5) THE VARIATION RATE

DWPT can benefit from two main features: constant system performances, such as power and efficiency, and constant control variables, such as frequency or phase shifts. Otherwise, tuning those variables is necessary for each k to achieve optimum performance. Similar to the power variation coefficient in [16], a variation rate is introduced

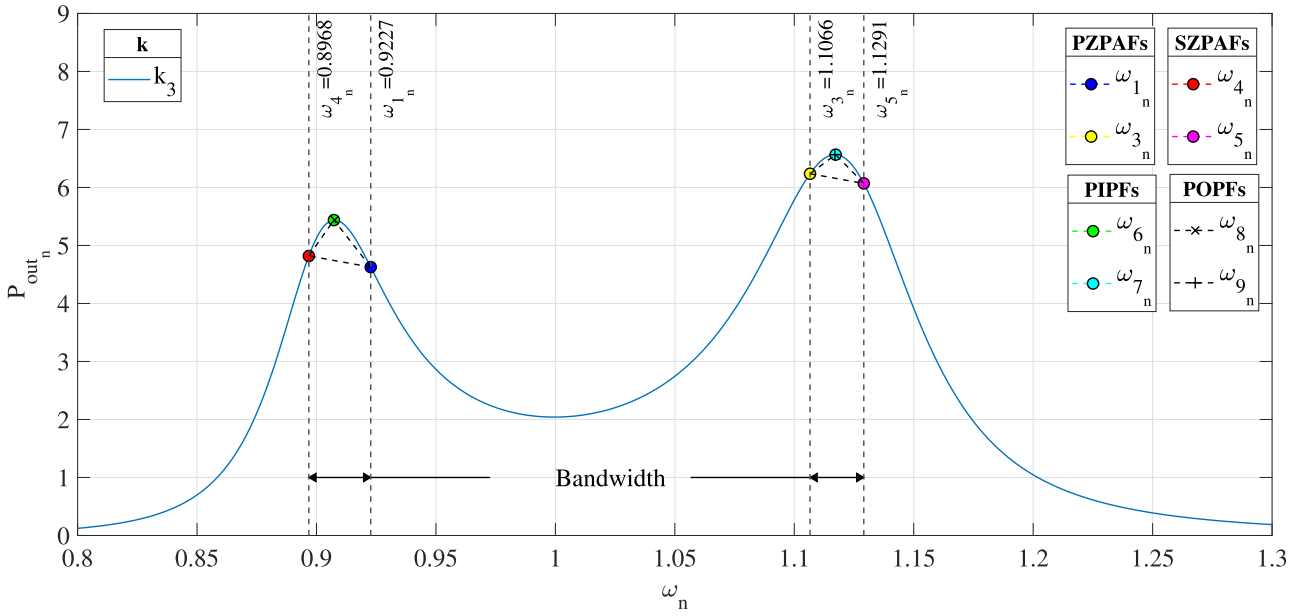

FIGURE 17. Power triangle and bandwidth.

TABLE 3. The bandwidth of power triangle.

MFBW (%)	0.11	0.165	0.225	0.306	0.396	0.496	0.581	Mean
Group A	NaN	NaN	1.43	0.91	0.67	0.52	0.44	0.80
θ_1	NaN	NaN	96.59	97.39	98.61	98.44	99.38	98.08
θ_2	NaN	NaN	109.30	103.87	103.31	102.61	102.96	104.41
θ_{12}	NaN	NaN	12.82	6.50	3.95	2.57	1.94	5.55
Group B	1.76	1.37	1.01	0.74	0.58	0.46	0.40	0.90
θ_1	170.94	119.91	110.37	107.01	105.07	104.56	103.82	117.38
θ_2	23.83	14.12	9.31	6.23	4.41	3.17	2.44	9.07
θ_{12}	7.92	3.26	1.29	0.48	0.20	0.09	0.05	1.90

to quantify and qualify how big variations different control variables have to make in order to achieve optimum system performances across the entire range of k, given in (13).

$$F = \frac{max(signal) - min(signal)}{max(signal)} \times 100 \qquad (13)$$

where *signal* refers to ω_{o_n}, P_{in_n}, P_{out_n}, η, θ_1 or θ_2.

Table 4 summarizes the variation rates for all the normalized optimum frequencies, ω_{o_n}, in terms of P_{in_n}, P_{out_n}, θ_1, θ_2 and θ_{12}, for the entire range of k suitable for DWPT applications, from 0.225 to 0.581 while avoiding power surge in low coupling situations. The quality indicator is considered low when the variation rate is below 10%, medium when the rate is between 10% to 30%, and high when the rate is higher than 30%, respectively.

Overall, the system can achieve stable efficiency at all the normalized optimum frequencies for the whole range of k. ω_{1_n} is the most popular choice for ZPA control in the literature because of its lower values in frequency, compared to ω_{3_n}, leading to lower switching losses and, therefore, less demand on the power semi-conduction devices. Since it has a medium variation rate, a power regulation control should be added to maintain a relatively constant power for the range of k. However, considering the two ideal features for controlling DWPT, ω_{3_n}, ω_{4_n} and ω_{5_n} are most suitable for ZPA control, with low variation rates in the system performances.

On the other hand, ω_{2_n} has a high variation rate in the P_{in_n} and P_{out_n}, which is another reason why it is not suitable for power transfer control besides low power performances. However, due to its low variation rate in control parameters, it is undemanding to control when k changes and thus it is good for soft turn-on/off or being an initial frequency for the frequency sweeping method. Compared to ω_{2_n}, ω_{6_n} and ω_{8_n} have relatively higher variation rates across different control parameters. Therefore, the power and efficiency can be used as the condition to tune the corresponding ω_{o_n} by using the power tracking or efficiency tracking method. Both ω_{7_n} and ω_{9_n} have a medium variation rate in P_{in_n} and P_{out_n} but only slightly higher than the upper limit of low variation rate. Their low variation rates of θ_2 make them good candidates as the control variables for a phase shift control method.

V. VALIDATION

In this section, we validate the theoretical results by simulation and experiment. To compare the results for all normalized frequencies, the coupling coefficient, k, is selected between 0.225 to 0.581, where all normalized optimum frequencies exist. Moreover, the difference between PIPFs and POPFs is less than 50 Hz, which is too small to be distinguished in the experimental measurements. Therefore, only the POPFs are chosen for validation as the normalized output power reflects the effect of the total losses in the SSWPT circuit. Besides, only θ_2 is selected for validation since it is related to the other two phase shifts and more appropriate for measurements because of significantly larger differences in phase shifts for the normalized frequencies between Group A and Group B.

TABLE 4. The variation rates.

	System performance						Control parameter							
	P_{in_n}		P_{out_n}		η		ω_{o_n}		θ_1		θ_2		θ_{12}	
	F	Q	F	Q	F	Q	F	Q	F	Q	F	Q	F	Q
ω_{1_n}	11.324	M	11.084	M	0.270	L	13.656	M	0.000	Z	61.156	H	61.156	H
ω_{4_n}	6.796	L	7.483	L	0.736	L	11.942	M	52.335	H	0.000	Z	52.335	H
ω_{6_n}	2.399	L	2.169	L	0.281	L	12.598	M	53.175	H	58.715	H	56.083	H
ω_{8_n}	2.393	L	2.173	L	0.270	L	12.616	M	53.356	H	58.614	H	56.184	H
ω_{2_n}	85.321	H	85.200	H	0.818	L	0.751	L	0.000	Z	7.053	L	7.053	L
ω_{3_n}	8.682	L	8.452	L	0.251	L	27.331	M	0.000	Z	12.740	M	12.758	M
ω_{5_n}	6.855	L	6.059	L	0.848	L	26.438	M	68.185	H	0.000	Z	10.589	M
ω_{7_n}	13.075	M	12.613	M	0.528	L	26.907	M	66.520	H	6.743	L	11.641	M
ω_{9_n}	13.071	M	12.617	M	0.520	L	26.922	M	66.087	H	6.941	L	11.671	M

* Note: F– variation rate; Q– Qualitative indicator; L– Low; M– Medium; H – High; Z– Zero.

A. SIMULATION

A time-domain model of the SSWPT circuit is built in MATLAB/SIMULINK. The phase shifts are measured between the two waveforms of the normalized input voltage and the normalized output current. The normalized output power in the Time Domain (TD) simulation, $P^S_{out_n}$, is given in (14), expressed as the mean value of the square of the normalized output current, y_2, over a half period multiplied by the normalized impedance of the load resistance, $Z_{R_{L_n}}$.

$$P^S_{out_n} = Z_{R_{L_n}} \frac{\omega_n}{\pi} \int_0^{\frac{\pi}{\omega_n}} {y_2}^2(\theta_n) d\theta_n \tag{14}$$

B. EXPERIMENT

The experimental setup is composed of a resonance inverter, two coils, and a resistive load, as shown in Figure 18. The waveform generator generates the control signals to drive the 650 V CoolSiC™ MOSFETs (IMW65R048M1H) for a 20 kW prototype. Power analyzers are used for measuring the output power. Oscilloscope A is used to observe the two waveforms, the input voltage and the output current measured by the current probe, to find the PZPAFs and SZPAFs. θ_1 and θ_2 are measured using the cursor function of the oscilloscope. During the experiments, the control frequencies were alternated manually to search the POPFs between the PZPAFs and the SZPAFs. To mimic different dynamic situations, one coil is manually moved away from the other horizontally at five different distances, resulting in five changing coupling coefficients between two coils, which are then used to virtually construct the couple-coefficient curve across the whole range of misalignment situations. In this way, one can thoroughly understand the potential impact of changing coupling coefficients on system performances under dynamic situations.

Due to the normalization of the theoretical model and simulation model, the characteristic parameters of the system are not affected by the input power. Thus, it is sufficient to supply 100 V input voltage across E, equating to an input power of 1 kW, to the system during the experiments. The conversion from the measured output power, P_{out}, to the experimental normalized output power, $P^E_{out_n}$, is given in (15).

$$P^E_{out_n} = \frac{Z_1}{E^2} P_{out} \tag{15}$$

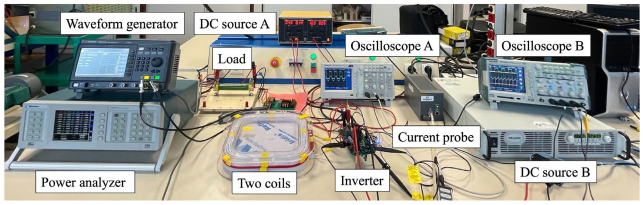

FIGURE 18. Experimental set-up.

C. VALIDATION RESULTS

Table 5 gives a thorough comparison of the normalized optimum frequencies, the normalized output power, P_{out_n}, and the phase shift, θ_2, between the theoretical, simulation and experimental results, with respect to the PZPAFs, ω_{1_n} and ω_{3_n}, the SZPAFs, ω_{4_n} and ω_{5_n}, and the POPFs, ω_{8_n} and ω_{9_n}. The results are also depicted in Figure 19.

The NRMSEs show the theoretical, simulation, and experimental results are in close proximity. Especially, the results of the theoretical FD model and the TD model in simulation are almost identical. During the experiment, Group B is slightly less precise compared to the frequencies in Group A, as their frequencies are higher. Compared to a lower frequency, a higher frequency has fewer samples with the same sampling rate, resulting in higher NRMSEs in most cases. The average NRMSEs for ω_{1_n}, ω_{3_n}, ω_{4_n}, ω_{5_n}, ω_{8_n} and ω_{9_n} are 0.129%, 1.459%, 0.0894%, 1.118%, 0.0966% and 1.16% respectively, which are less than 1.5%, as shown in the first column of Figure 19. The average NRMSEs of P_{out_n} for ω_{1_n}, ω_{3_n}, ω_{4_n}, ω_{5_n}, ω_{8_n} and ω_{9_n} are 1.445%, 0.337%, 1.111%, 0.308%, 0.952% and 0.619% respectively, which are less than 1.5% as well, as shown in the second column of Figure 19. Similarly, the average NRMSEs of θ_2 for ω_{1_n}, ω_{3_n}, ω_{4_n}, ω_{5_n}, ω_{8_n} and ω_{9_n} are 6.176%, 0.740%, 0.014%, 11.882% and 1.056% respectively, which varies largely in between the results, as shown in the third column of Figure 19. The cross-validation of the optimum frequencies and their related system performances are in agreement with each other considering the existence of some uncertainties which is common during validation, such as (1) the sampling rates being different in the theoretical model, simulation model, and measurement from the oscilloscope; (2) the resolution of the oscilloscope trace for zero-crossing determination;

TABLE 5. The power and the phase shift of the normalized optimum frequencies from a theoretical model, simulation model, and experiment.

	k	0.225	0.306	0.396	0.496	0.581	k	0.225	0.306	0.396	0.496	0.581
T	ω_{1_n}	0.9227	0.8847	0.8517	0.8203	0.7967	ω_{3_n}	1.1066	1.1753	1.2639	1.3867	1.5228
S	ω_{1_n}	0.9227	0.8847	0.8517	0.8203	0.7967	ω_{3_n}	1.1066	1.1753	1.2639	1.3867	1.5228
E	ω_{1_n}	0.9219	0.8865	0.8530	0.8174	0.7920	ω_{3_n}	1.0814	1.1424	1.2236	1.3302	1.4775
	$\varepsilon(\%)$	0.041	0.095	0.070	0.165	0.276	$\varepsilon(\%)$	1.080	1.333	1.519	1.946	1.418
T	P_{out_n}	4.627	4.938	5.072	5.160	5.204	P_{out_n}	6.237	5.973	5.840	5.756	5.709
S	P_{out_n}	4.626	4.938	5.072	5.162	5.209	P_{out_n}	6.235	5.972	5.838	5.754	5.708
E	P_{out_n}	5.056	5.182	5.061	5.207	5.189	P_{out_n}	6.244	5.932	5.798	5.677	5.748
	$\varepsilon(\%)$	4.247	2.288	0.099	0.424	0.164	$\varepsilon(\%)$	0.061	0.322	0.334	0.640	0.325
T	$\theta_2(^\circ)$	45.41	31.86	24.84	20.15	17.64	$\theta_2(^\circ)$	149.62	158.96	164.90	169.03	171.46
S	$\theta_2(^\circ)$	46.22	33.55	26.34	21.87	17.72	$\theta_2(^\circ)$	148.96	156.70	161.49	164.63	169.45
E	$\theta_2(^\circ)$	47.07	30.16	24.19	17.38	13.48	$\theta_2(^\circ)$	150.29	157.16	161.38	166	171.79
	$\varepsilon(\%)$	1.462	4.345	3.584	9.335	12.156	$\varepsilon(\%)$	0.365	0.620	1.005	1.104	0.605
T	ω_{4_n}	0.8968	0.8687	0.8403	0.8118	0.7897	ω_{5_n}	1.1291	1.1929	1.2786	1.3996	1.5349
S	ω_{n4}	0.8968	0.8687	0.8403	0.8118	0.7897	ω_{5_n}	1.1291	1.1929	1.2786	1.3996	1.5349
E	ω_{4_n}	0.8926	0.8682	0.8408	0.8119	0.7870	ω_{5_n}	1.1068	1.1657	1.2490	1.3607	1.4978
	$\varepsilon(\%)$	0.223	0.027	0.027	0.006	0.164	$\varepsilon(\%)$	0.936	1.082	1.100	1.323	1.150
T	P_{out_n}	4.819	4.988	5.093	5.167	5.209	P_{out_n}	6.070	5.916	5.812	5.742	5.702
S	P_{out_n}	4.818	4.987	5.093	5.168	5.213	P_{out_n}	6.066	5.913	5.810	5.740	5.700
E	P_{out_n}	4.465	4.920	5.037	5.189	5.138	P_{out_n}	6.031	5.948	5.831	5.830	5.713
	$\varepsilon(\%)$	3.544	0.637	0.517	0.193	0.661	$\varepsilon(\%)$	0.286	0.266	0.159	0.728	0.102
T	$\theta_2(^\circ)$	0.11	0.09	0.03	0.03	0.00	$\theta_2(^\circ)$	180.07	180.01	180.07	180.07	180.04
S	$\theta_2(^\circ)$	0.00	0.00	0.00	0.00	-1.37	$\theta_2(^\circ)$	180.05	180.04	180.06	180.05	180.03
E	$\theta_2(^\circ)$	0.00	0.00	0.00	0.00	0.00	$\theta_2(^\circ)$	180.00	180.00	180.00	180.00	180.00
	$\varepsilon(\%)$	NaN	NaN	NaN	NaN	NaN	$\varepsilon(\%)$	0.016	0.010	0.018	0.017	0.009
T	ω_{8_n}	0.9076	0.8761	0.8457	0.8159	0.7931	ω_{9_n}	1.1170	1.1835	1.2708	1.3927	1.5285
S	ω_{n8}	0.9076	0.8761	0.8457	0.8159	0.7931	ω_{9_n}	1.1170	1.1835	1.2708	1.3927	1.5285
E	ω_{n8}	0.9098	0.8784	0.8469	0.8149	0.7910	ω_{9_n}	1.0977	1.1525	1.2388	1.3556	1.4876
	$\varepsilon(\%)$	0.116	0.121	0.065	0.058	0.123	$\varepsilon(\%)$	0.820	1.245	1.196	1.267	1.272
T	P_{out_n}	5.438	5.341	5.320	5.323	5.330	P_{out_n}	6.566	6.140	5.927	5.802	5.737
S	P_{out_n}	5.438	5.340	5.320	5.323	5.333	P_{out_n}	6.564	6.137	5.926	5.800	5.736
E	P_{out_n}	5.707	5.352	5.262	5.238	5.210	P_{out_n}	6.537	6.231	6.054	5.881	5.800
	$\varepsilon(\%)$	2.294	0.106	0.517	0.757	1.085	$\varepsilon(\%)$	0.204	0.711	1.011	0.650	0.517
T	$\theta_2(^\circ)$	21.01	15.50	12.12	9.92	8.47	$\theta_2(^\circ)$	163.32	168.65	171.99	174.16	175.50
S	$\theta_2(^\circ)$	21.99	16.66	13.26	10.07	8.07	$\theta_2(^\circ)$	163.73	165.16	169.66	172.29	174.03
E	$\theta_2(^\circ)$	29.67	22.42	15.61	12.71	8.97	$\theta_2(^\circ)$	166.59	166.71	163.39	174.95	177.22
	$\varepsilon(\%)$	16.000	16.635	10.647	11.752	4.378	$\varepsilon(\%)$	0.885	0.856	2.156	0.642	0.741

* Note: T— Theoretical model; S- — Simulation model; E — Experiment; ε — NRMSE.

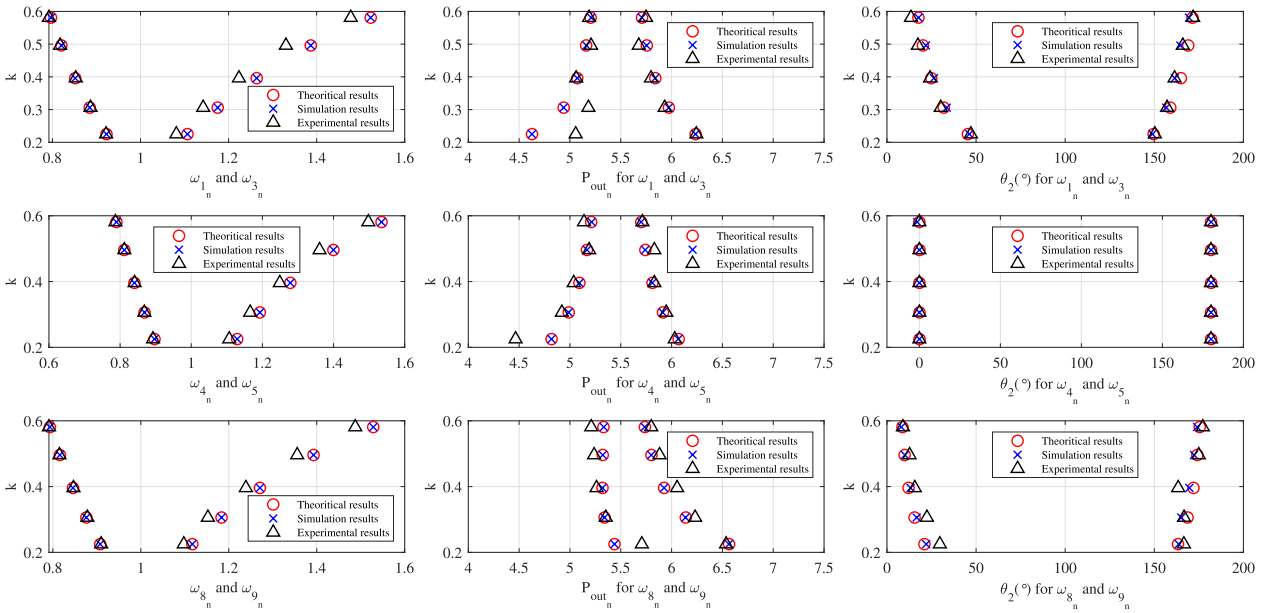

FIGURE 19. The comparison of the theoretical, simulation, and experimental results.

(3) the small changes in frequencies which can result in big variations in the phase shifts and output power due to the sensitivity of the resonance system and (4) the simplified SSWPT system model by ignoring all the losses caused by switching, cables, and other parasitic elements in the system, etc.

VI. CONCLUSION

The frequency and phase shift have great influences on the power and energy efficiency of the DWPT system under different misalignment situations. More specifically, following a thorough frequency domain analysis of a general SSWPT system, we identified four types of optimum frequencies, namely PZPAFs, SZPAFs, PIPFs, and POPFs, which included nine frequencies and can be separated into three groups according to the ratio between the primary and secondary resonant frequencies. They varied dynamically when the coupling coefficient changed. A detailed comparison showed the optimal frequencies in the same group perform similarly, while differences existed between different groups. Different frequencies may be utilized to satisfy the specific need for control under different situations. The same frequencies have three different phase shifts, which provide options for phase shift control methods. Interestingly, a power-triangle relationship was discovered during the study, which can be conveniently used to track and identify the wider range of the potential optimum frequencies and phase shifts as control variables to maximize the power transfer of an SSWPT system. The comprehensive and cross-validated frequency-domain analysis could provide the readers valuable insights into the relationship between frequency, phase shift, and power under dynamic situations, and hence lay a foundation for developing robust control strategies in future DWPT research and practical applications. Specifically, from a practical application perspective, the developed theoretical and simulation models would be beneficial when addressing the potential impact of changed characteristic parameters and coupling coefficients on the performance of the DWPT systems, which may be caused, for example, by the variation or aging of system components and the ever-changing operating environments, respectively.

REFERENCES

[1] (2023). *IEA, Electric Car Sales, 2016–2023 (Licence: CC by 4.0)*. International Energy Agency, Paris. [Online]. Available: https://www.iea.org/data-and-statistics/charts/electric-car-sales-2016-2023

[2] S. B.-S. K. Bond. (Sep. 2023). *X-Change: Cars the End of the ICE Age*. [Online]. Available: https://rmi.org/insight/x-change-cars/

[3] C. C. Mi, G. Buja, S. Y. Choi, and C. T. Rim, "Modern advances in wireless power transfer systems for roadway powered electric vehicles," *IEEE Trans. Ind. Electron.*, vol. 63, no. 10, pp. 6533–6545, Oct. 2016.

[4] G. A. Covic and J. T. Boys, "Modern trends in inductive power transfer for transportation applications," *IEEE J. Emerg. Sel. Topics Power Electron.*, vol. 1, no. 1, pp. 28–41, Mar. 2013.

[5] Y. J. Jang, "Survey of the operation and system study on wireless charging electric vehicle systems," *Transp. Res. Part C: Emerg. Technol.*, vol. 95, pp. 844–866, Oct. 2018. [Online]. Available: https://www.sciencedirect.com/science/article/pii/S0968090X18304649

[6] *Electric Vehicle Wireless Power Transfer (WPT) Systems—Part 3: Specific Requirements for the Magnetic Field Wireless Power Transfer Systems*, Standard IEC 61980-3, Int. Electrotechnical Commission, Nov. 2022.

[7] A. Mahesh, B. Chokkalingam, and L. Mihet-Popa, "Inductive wireless power transfer charging for electric vehicles—A review," *IEEE Access*, vol. 9, pp. 137667–137713, 2021.

[8] K. Chen and Z. Zhang, "In-flight wireless charging: A promising application-oriented charging technique for drones," *IEEE Ind. Electron. Mag.*, vol. 18, no. 1, pp. 6–16, Mar. 2024.

[9] A. Koran and K. Badran, "Adaptive frequency control of a sensorless-receiver inductive wireless power transfer system based on mixed-compensation topology," *IEEE Trans. Power Electron.*, vol. 36, no. 1, pp. 978–990, Jan. 2021.

[10] A. Babaki, S. Vaez-Zadeh, A. Zakerian, and G. A. Covic, "Variable-frequency retuned WPT system for power transfer and efficiency improvement in dynamic EV charging with fixed voltage characteristic," *IEEE Trans. Energy Convers.*, vol. 36, no. 3, pp. 2141–2151, Sep. 2021.

[11] Y. Zhang, T. Kan, Z. Yan, and C. C. Mi, "Frequency and voltage tuning of series–series compensated wireless power transfer system to sustain rated power under various conditions," *IEEE J. Emerg. Sel. Topics Power Electron.*, vol. 7, no. 2, pp. 1311–1317, Jun. 2019.

[12] C.-S. Wang, G. A. Covic, and O. H. Stielau, "Power transfer capability and bifurcation phenomena of loosely coupled inductive power transfer systems," *IEEE Trans. Ind. Electron.*, vol. 51, no. 1, pp. 148–157, Feb. 2004.

[13] W. Liu, K. T. Chau, C. H. T. Lee, W. Han, X. Tian, and W. H. Lam, "Full-range soft-switching pulse frequency modulated wireless power transfer," *IEEE Trans. Power Electron.*, vol. 35, no. 6, pp. 6533–6547, Jun. 2020.

[14] F. Chen, H. Garnier, Q. Deng, M. K. Kazimierczuk, and X. Zhuan, "Control-oriented modeling of wireless power transfer systems with phase-shift control," *IEEE Trans. Power Electron.*, vol. 35, no. 2, pp. 2119–2134, Feb. 2020.

[15] E. Gati, G. Kampitsis, I. Stavropoulos, S. Papathanassiou, and S. Manias, "Wireless phase–locked loop control for inductive power transfer systems," in *Proc. IEEE Appl. Power Electron. Conf. Expo. (APEC)*, Mar. 2015, pp. 1601–1607.

[16] Z. Yao, S. Luo, Z. Zhang, G. Li, X. Wei, X. Shen, N. Zhang, P. T. Krein, and H. Ma, "Analysis and design of multifrequency compensation strategy for wide misalignment tolerance in inductive power transfer systems," *IEEE Trans. Power Electron.*, vol. 38, no. 9, pp. 11705–11718, Sep. 2023.

[17] K. Chen, K. W. E. Cheng, Y. Yang, and J. Pan, "A fast self-positioning-based optimal frequency control for inductive wireless power transfer systems without communication," *IEEE Trans. Ind. Electron.*, vol. 70, no. 1, pp. 334–343, Jan. 2023.

[18] S.-Y. Cho, I.-O. Lee, S. Moon, G.-W. Moon, B.-C. Kim, and K. Y. Kim, "Series-series compensated wireless power transfer at two different resonant frequencies," in *Proc. IEEE ECCE Asia Downunder*, Jun. 2013, pp. 1052–1058.

[19] A. Laha, A. Kalathy, and P. Jain, "Frequency domain analysis of a wireless power transfer system operating in a wide load and coupling range using frequency modulation of inverter for voltage regulation," in *Proc. IEEE Appl. Power Electron. Conf. Expo. (APEC)*, Mar. 2022, pp. 1891–1897.

[20] M. Liang, K. E. Khamlichi Drissi, and C. Pasquier, "Optimal frequency for dynamic wireless power transfer," in *Proc. 24th Eur. Conf. Power Electron. Appl.*, Sep. 2022, pp. 1–10.

[21] Y. Lu and W. H. Ki, *CMOS Integrated Circuit Design for Wireless Power Transfer*. Singapore: Springer, 2018.

[22] M. Liang, K. El Khamlichi Drissi, and C. Pasquier, "Self- and mutual-inductance cross-validation of multi-turn, multi-layer square coils for dynamic wireless charging of electric vehicles," *Energies*, vol. 16, no. 20, p. 7033, Oct. 2023. [Online]. Available: https://www.mdpi.com/1996-1073/16/20/7033

[23] T. Ma, C. Q. Jiang, Y. Zhang, Y. Wang, Y. Cheng, and S. Cui, "Modeling and analysis of periodic energy control for series–series wireless power transfer system," *IEEE Trans. Power Electron.*, vol. 39, no. 4, pp. 4837–4849, Apr. 2024.

MINCUI LIANG received the Bachelor of Engineering degree from Shanghai Maritime University, China, and the Master of Philosophy degree from Newcastle University, U.K. She is currently pursuing the Doctor of Philosophy degree with the Pascal Institute, Clermont Auvergne University, France. Her research interests include WPT systems, resonance converters, advanced control, and artificial intelligence.

KHALIL EL KHAMLICHI DRISSI (Senior Member, IEEE) was born in Fez, Morocco, in 1965. He received the Diploma degree in electrical engineering and the M.Sc. degree from the École Centrale de Lille, in 1987, and the Ph.D. degree from the University of Lille, in 1990. He joined Polytech Clermont, in 1990, as an Associate Professor and became a Full Professor, in 2005. He was the Dean of the Electrical Engineering Department, from 2007 to 2011. He became the Vice President of Research and Innovation, from 2012 to 2016. Since 2017, he has been a Vice Regional Academic Delegate of Research and Innovation (Vice DRARI) for the Auvergne-Rhone-Alpes Region. He was appointed to the rank of knight in the order of academic palms, in 2020. He is currently an Expert for different French agencies (ANRT, ANR, HCERES, and DGRI). He is also the Project Leader and is also responsible for several international projects related to EMC (FP7 Marie Curie, Econet, Cogito, Integrafm, Cedre, Toubkal, and Tassili). He also has an on-going collaboration with different companies, such as Vedecom, IFPEN, EDF, France Telecom, and Landis+zGyr. He is also a Full Professor with Clermont Auvergne University. He has authored or coauthored more than 280 scientific papers published in peer-reviewed journals, presented at international conferences, and is the author of six WO patents. His research interests include EMC in power electronics and power systems, in particular numerical modeling, EMI reduction, converter control, and electromobility. He has been a Senior Member of IEEE Electromagnetic Compatibility and IEEE Power Electronics Societies, since 2018.

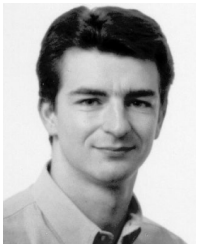

CHRISTOPHE PASQUIER was born in France, in 1972. He received the M.Sc. and Ph.D. degrees in electrical engineering from the University of Nantes, in 1996 and 2000, respectively. From 2000 to 2004, he was with the GE44 Team, University of Nantes, France. Since 2004, he has been an Associate Professor with the Department of Electrical Engineering, Polytech Clermont, Clermont Auvergne University, Clermont-Ferrand, France. Since 2005, he has been the Dean of the Department of Electrical Engineering. He is also a Researcher with the Institut Pascal Laboratory, where his research interests include electromagnetic compatibility, numerical modeling, power electronics, power systems, EMI reduction, and converter control. He is a member of the Society of Electricity, Communication, Electronics and Information Technologies, Auvergne, France.